UNIVERSITÀ DEGLI STUDI DI PADOVA

SCUOLA DI SCIENZE

DIPARTIMENTO DI GEOSCIENZE

Direttore Prof. Fabrizio Nestola

TESI DI LAUREA MAGISTRALE IN GEOLOGIA E GEOLOGIA TECNICA

AN EXPERIMENTAL APPARATUS FOR THE STUDY OF LOW ENTHALPY GEOTHERMAL ENERGY

Relatore

Prof. Paolo Scotton

Laureando

Riccardo Volpe

Anno Accademico 2018/2019

Abstract

This work has the goal to present an experimental apparatus designed for the study of the energy exchange that takes place between a geothermal probe and the surrounding environment, at low enthalpy conditions.

The experimental apparatus (installed in a thermostatic chamber inside the Geotechnical Engineering Laboratory of the University of Padua) has a volume of about $1m^3$ and is crossed by a copper thermal probe. The thermal probe is served by a closed hydraulic circuit. The flow rate and the fluid temperature, through the thermal probe, are imposed. Inside the granular material (*Risetta del Brenta*), that fills up the experimental apparatus, 24 high precision temperature sensors are properly distributed. The experimental apparatus can be saturated with water and a filtration motion can be realized using a second hydraulic circuit.

The first part of this work is dedicated to an introduction to the basic theory useful for the processing carried out, and to a detailed description of the physical model.

Subsequently a test is taken into consideration, carried out in the absence of

intergranular water. The fundamental properties of the obtained acquisitions are described, the reliability of its behavior and the validity of the initial hypothesis are verified. At last, the power of the thermal probe is estimated and the temperature field, generated by the latter, inside the control volume is described.

Riassunto

Il presente lavoro di tesi ha lo scopo di presentare un apparato sperimentale progettato per lo studio dello scambio energetico che si verifica tra una sonda geotermica e l'ambiente circostante, in condizioni di bassa entalpia.

L'apparato sperimentale (installato in una camera termostatica nel laboratorio di Ingegneria Geotecnica dell'Università di Padova) ha un volume di circa $1m^3$ ed è attraversato da una sonda termica realizzata in rame. La sonda termica è servita da un circuito idraulico chiuso. La portata idrica, che attraversa la sonda termica, viene impostata, così come la temperatura del fluido. Nel materiale granulare (*Risetta del Brenta*), che riempie l'apparato sperimentale, sono opportunamente distribuite 24 sonde di temperatura di elevata precisione. L'apparato sperimentale può essere saturato con acqua e può essere realizzato un moto di filtrazione mediante l'utilizzo di un secondo circuito idraulico.

La prima parte dell'elaborato è dedicata all'introduzione della teoria di base utile alle elaborazioni svolte, nonchè ad una dettagliata descrizione del modello fisico.

Successivamente viene preso in esame un test, svolto in assenza di acqua intergranulare. Vengono descritte le proprietà fondamentali delle acquisizioni ottenute, verificata l'affidabilità del suo comportamento e la validità delle ipotesi fatte. In ultimo, viene stimata la potenza della sonda termica e viene descritto il campo di temperatura generato da quest'ultima all'interno del volume di controllo.

Contents

List of Figures

List of Tables

Introduction

The design and sizing of a borehole heat exchanger (BHE) used in a shallow geothermal system is done by evaluating the thermal energy exchange capacity of the system itself composed by the BHE and the surrounding ground.

In turn, the thermal energy exchange capacity mainly depends on the thermal properties of the sediments and on possible groundwater flow (Sutton, Nutter, & Couvillion, 2003).

Another important aspect is that the continuous thermal energy exchange in the geothermal system modifies the thermal gradient around the BHE.

Different approaches can be used to model a BHE such as analytical ones (Philippe, Bernier, & Marchio, 2009) or numerical ones (Al-Khoury, Bonnier, & Brinkgreve, 2005; Al-Khoury & Bonnier, 2006).

There are also known examples of modeling focusing on teleheating (district heating) (Carlini, Castellucci, Allegrini, & Tucci, 2012).

In any case models of heat transfer and groundwater flow are used to evaluate the thermal alteration in the ground and the BHE performance.

These models are validated by comparison with experimental data which are as crucial as difficult to obtain due to often challenging on field measurements. A bad quality of data from on field measurements may lead to a not enough accurate design of a BHE which, in turn, brings to abate the economic and environmental benefits of the whole geothermal system.
The use of physical models can be resolutive for the study of many natural phenomena that may be hard to solve analytically or numerically (Green, 2014; Volkov, Ryzhenkov, Kurshakov, Grigoriev, & Bekker, 2017) or to verify the results obtained from these methods.

A physical model performs well also when used to describe the hydro-thermodynamic interaction between a thermal probe and the surrounding environment it exchanges energy with, for example by studying this interaction in case of ground freezing phenomena (Wang, Gao, Zhu, Yu, & Zhao, 2013).

The physical model used in this work was built (Scotton, 2017) for the study and measurement, under controlled conditions, of the evolution in space and time of the thermal alteration induced in the ground by a thermal probe. Precisely a thermal probe has been inserted in a volume of roughly 1 m^3 in which 24 high precision temperature sensors had been distributed at different distances from the probe. A wide range of configurations are possible in terms of different materials filling the volume (with their different porosity, thermal properties and hydraulic permeability), groundwater flow conditions and thermal probe operations (Scotton, Teza, Rossi, Dalla Santa, & Galgaro,

2018).

The following work will introduce the physical model, explain the configuration of the experimental apparatus, display the collected data in one experimental configuration, show the results obtained by the test and discuss the potentialities and limits of the physical model.

Chapter 1

Theoretical Foundations

1.1 Dimensional Analysis

Through the dimensional analysis, applied to the problem of energy transport in a porous medium saturated with moving filtration fluid, five dimensionless groups can be determined (Figure 1.1). Reynolds number represents the ratio between inertial forces and viscous forces, thus it gives information about the flow regime, laminar or turbulent; Prandtl number establishes the importance of cinematic diffusivity with respect to thermal diffusivity; Nusselt number represents the relative importance of the convective energy transport terms with respect to the conductive terms. The other two parameters describe the thermal conductivity and thermal capacity ratios of the fluid and the solid parts that constitute the porous medium-filtration fluid system.

The dimensional analysis applied to the problem of energy transport in a pipe generates the three dimensionless groups of Figure 1.2, the physical meaning of the parameters is the same previously described except this time they are referred to the fluid inside the pipe.

N. Reynolds $\Pi_1 = \frac{\rho_f \cdot V_f \cdot d}{\mu_f}$ N. Prandtl $\Pi_2 = \frac{C_{pf} \cdot \mu_f}{\lambda_f}$ N. Nusselt $\Pi_3 = \frac{\alpha\, d}{\lambda_f}$

$\Pi_4 = \frac{\lambda_f}{\lambda_s}$ $\Pi_5 = \frac{C_{pf}}{C_{ps}}$

Figure 1.1: The numbers obtained by the dimensional analysis of the energy transport phenomenon in a porous medium saturated with moving filtration fluid.

N. Reynolds $\Pi_1 = \frac{\rho_c \cdot V_c \cdot d_c}{\mu_c}$ N. Prandtl $\Pi_2 = \frac{C_{pc} \cdot \mu_c}{\lambda_c}$ N. Nusselt $\Pi_3 = \frac{\alpha_c d_c}{\lambda_c}$

Figure 1.2: The numbers obtained by the dimensional analysis of the energy transport phenomenon in a fluid inside a pipe.

The goal of the physical model is the experimental description of the energy balance (equation (1.1)) generated when the thermal probe yields or receives thermal energy to or from the surrounding environment that, in turn, receives or yields thermal energy to the probe fluid.

$$(h_1 + gz_1 + \frac{V_1^2}{2})\dot{m}_1 - (h_2 + gz_2 + \frac{V_2^2}{2})\dot{m}_2 - \dot{Q} = \frac{dE}{dt} \qquad (1.1)$$

In equation (1.1) h_1 and h_2 represent the enthalpy of the filtration fluid at the input and output of the control volume occupied by the porous medium,

V is the velocity, $\dot{m}$ is the mass flow rate, $\dot{Q}$ is the heat flux generated inside the control volume and E is the energy inside the control volume.

1.2 Thermodynamic Process

The flow meter measures the volumetric flow rate in the thermal probe at a temperature that is hypothesized equal to the temperature of the probe inlet fluid, from that the velocity of the probe fluid is determined.

The energy balance equation is written as follows:

$$(h_1 + gz_1 + \frac{V_1^2}{2})\dot{m}_1 - (h_2 + gz_2 + \frac{V_2^2}{2})\dot{m}_2 + W_t - W_m + \dot{Q} = \frac{dE}{dt}$$

Where h_i is the inlet and outlet fluid enthalpy per mass unit; gz_i is the potential energy owned by the inlet and outlet fluid per mass unit; $\frac{V_i^2}{2}$ is the kinetic energy of a mass unit entering or leaving the system; $\dot{m}_i$ is the mass flow rate; W_t is the thermal power exchanged by the system; W_m is the mechanical power exchanged by the system and $\frac{dE}{dt}$ is the energy variation, in time, inside the thermal probe thermodynamic system.

The thermal power generated inside the system ($\dot{Q}$) is nil. The net mechanical power exchanged by the system (W_m) is nil. Thus the equation becomes:

$$(h_1 + gz_1 + \frac{V_1^2}{2})\dot{m}_1 - (h_2 + gz_2 + \frac{V_2^2}{2})\dot{m}_2 + W_t = \frac{dE}{dt}$$

Considering that the enthalpy is a function of the internal energy and the mass flow rate as a constant, then the energy balance can be written as follows:

$$(u_1 + p_1 \cdot v_1 + gz_1 + \frac{V_1^2}{2})\dot{m} - (u_2 + p_2 \cdot v_2 + gz_2 + \frac{V_2^2}{2})\dot{m} + W_t = \frac{dE}{dt}$$

$$(u_1 - u_2)\dot{m} + (\frac{p_1}{\rho_1} - \frac{p_2}{\rho_2})\dot{m} + g(z_1 - z_2)\dot{m} + (\frac{V_1^2}{2} - \frac{V_2^2}{2})\dot{m} + W_t = \frac{dE}{dt}$$

In the case of hydrostatics pressure distribution inside the probe, thus considering stationary motion, and small energy dissipation due to friction, the pressure p_2 can be written as follows:

$$p_2 \backsimeq p_1 + \frac{\int_{z_2}^{z_1} g \cdot \rho \cdot dVol}{S} = p_1 + \frac{\int_{z_2}^{z_1} g \cdot \rho \cdot S \cdot dz}{S} = p_1 + \int_{z_2}^{z_1} g \cdot \rho \cdot dz$$

Where Vol is the volume of the fluid inside the thermal probe, S is the area of the probe section and ρ is the density of the probe fluid that varies with temperature along the thermal probe.

If a linear temperature variation along the probe is hypothesized and, consequently, a linear density variation, the following is obtained:

$$p_2 \backsimeq p_1 + g \cdot \frac{\rho(z_1) + \rho(z_2)}{2} \cdot (z_1 - z_2) = p_1 + g \cdot \frac{\rho_1 + \rho_2}{2} \cdot (z_1 - z_2)$$

Considering that the density variation along the probe is low, due to a limited temperature variation, then $\rho_1 \backsimeq \rho_2 = \rho$ and $V_1 \backsimeq V_2 = V$. Replacing

in the energy equation the following is obtained:

$$(u_1-u_2)\dot{m}+(\frac{p_1}{\rho}-\frac{p_1+g\cdot\rho(z_1-z_2)}{\rho})\dot{m}+g(z_1-z_2)\dot{m}+(\frac{V}{2}-\frac{V}{2})\dot{m}+W_t=\frac{dE}{dt}$$

$$(u_1-u_2)\dot{m}+W_t=\frac{dE}{dt}$$

Integrating in a finite time interval Δt:

$$\int_t^{t+\Delta t}(u_1-u_2)\cdot\dot{m}\cdot dt+\int_t^{t+\Delta t}W_t\cdot dt=\int_t^{t+\Delta t}\frac{dE}{dt}\cdot dt=E(t+\Delta t)-E(t)$$

In case the various terms considered are constant in the time interval considered:

$$(u_1-u_2)m\cdot\Delta t+W_t\cdot\Delta t=E(t+\Delta t)-E(t)$$

Thus, the exchanged energy by the system with the surrounding environment is:

$$W_t\cdot\Delta t=-(u_1-u_2)\dot{m}\cdot\Delta t+E(t+\Delta t)-E(t) \tag{1.2}$$

The energy in the control volume, at a certain time, can be written treating the various components as the mean value between the inlet value (subscript 1) and the outlet value (subscript 2) in the control volume, as follows:

$$E(t)=[\frac{u_1(t)+u_2(t)}{2}+\frac{1}{2}(\frac{V_1(t)^2+V_2(t)^2}{2})+g(\frac{z_1+z_2}{2})]\cdot\frac{\rho_1(t)+\rho_2(t)}{2}\cdot Vol$$

1.3 Heat Conduction Theory

Heat transfer can occur in three different mechanisms: conduction, convection and radiation. Thermal conduction is the transfer of thermal energy, without apparent movement of matter, from regions at higher temperature to regions at lower temperature by collisions of particles and movement of electrons within a solid, liquid or gaseous body. A simple scheme of this mechanism is displayed in Figure 1.3.

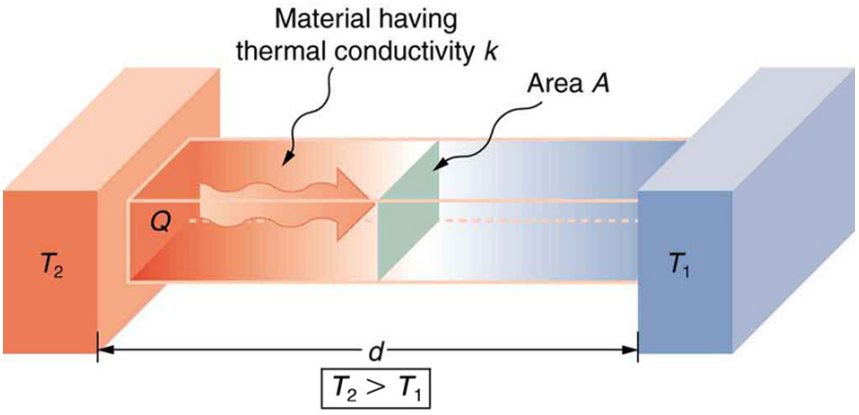

Figure 1.3: Simple representation of heat conduction. (M. Williams, Universe Today, 2014).

The fundamental heat conduction law is:

$$q = -\lambda \cdot A \cdot \frac{dT}{dx}, (Fourier, 1955) \tag{1.3}$$

where λ is the thermal conductivity of the body (also called k), A is the area of the surface orthogonal to the heat flux and $\frac{dT}{dx}$ is the temperature gradient.

To apply the heat conduction theory some assumptions have been made:

1. Continuous medium: its physical properties do not present discontinuities of any species;

2. Uniform medium: each point behaves in the same manner (same physical properties);

3. Isotropic medium: its physical properties do not depend on the considered direction.

The energy accumulated in an elementary cubic volume can be calculated considering that it equals to the incoming energy plus the generated internal energy subtracted of the outgoing energy (Figure 1.4). This can be written for one direction, say x:

$$\begin{cases} dq_x = -\lambda \cdot (dy \cdot dz) \cdot \dfrac{\partial T}{\partial x} \\ dq_{x+dx} = dq_x + (\dfrac{\partial}{\partial x} \cdot dq_x)dx \end{cases}$$

It can also be written for the three directions (x, y and z) as follows:

$$\begin{cases} dq_x - dq_{x+dx} = \dfrac{\partial}{\partial x}(\lambda \cdot \dfrac{\partial T}{\partial x})dxdydz \\ dq_y - dq_{y+dy} = \dfrac{\partial}{\partial y}(\lambda \cdot \dfrac{\partial T}{\partial y})dxdydz \\ dq_z - dq_{z+dz} = \dfrac{\partial}{\partial z}(\lambda \cdot \dfrac{\partial T}{\partial z})dxdydz \end{cases}$$

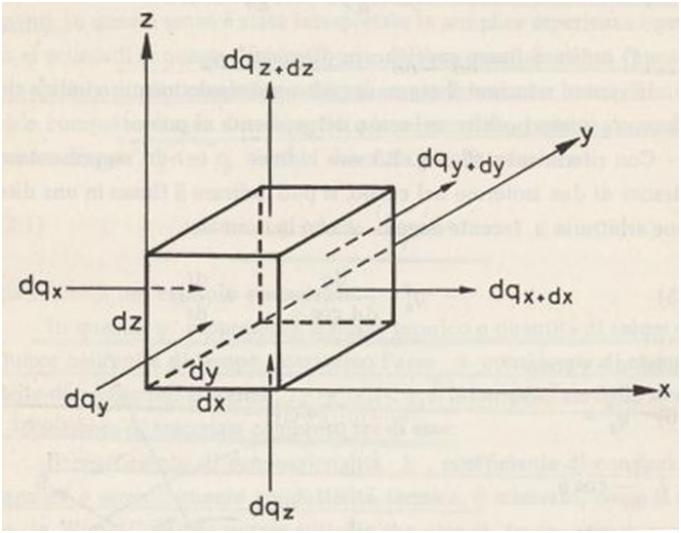

Figure 1.4: Energy balance for an elementary cubic volume in the x, y and z direction.

The increase of internal energy in a time unit can be calculated considering that the specific internal energy (u) is a function of temperature and specific volume: $u = f(T, v)$

Thus, the specific heat per unit of volume (c_v) is:

$$c_v = (\frac{\partial u}{\partial T})_v$$

So if the initial specific internal energy is u, then the final specific internal energy is:

$$u + \frac{\partial}{\partial t} \cdot u \cdot dt = u + (\frac{\partial u}{\partial T})_v \cdot dT + (\frac{\partial u}{\partial v})_T \cdot dv$$

The total energy balance, simplifying each term by $dxdydz$, can be written as:

$$\rho \cdot c_v \cdot \frac{\partial T}{\partial t} = [\frac{\partial}{\partial x}(\lambda \frac{\partial T}{\partial x}) + \frac{\partial}{\partial y}(\lambda \frac{\partial T}{\partial y}) + \frac{\partial}{\partial z}(\lambda \frac{\partial T}{\partial z})] + H$$

Where H is the internal energy generated in a time and volume unit.

If λ, c_v and v are independent from the considered point coordinates, then:

$$\frac{\partial T}{\partial t} = \frac{\lambda}{\rho \cdot c_v} \cdot [\frac{\partial}{\partial x}(\frac{\partial T}{\partial x}) + \frac{\partial}{\partial y}(\frac{\partial T}{\partial y}) + \frac{\partial}{\partial z}(\frac{\partial T}{\partial z})] + \frac{H}{\rho \cdot c_v} = a \cdot \nabla^2 T + \frac{H}{\rho \cdot c_v}$$

Where $a = \dfrac{\lambda}{\rho \cdot c_v}$ is the thermal diffusivity of the body.

In case of absence of internal energy generation, as it happens in the physical model, H equals to zero. Thus the energy balance becomes:

$$\frac{\partial T}{\partial t} = a \cdot \nabla^2 T, \text{(Fourier's equation)} \tag{1.4}$$

If the temperature is constant in time (steady state conditions) one can write Poisson's equation:

$$\nabla^2 T + \frac{H}{\lambda} = 0. \tag{1.5}$$

And, in case of zero energy generation inside the control volume, one can write Laplace's equation:

$$\frac{\partial^2 T}{\partial x^2} + \frac{\partial^2 T}{\partial y^2} + \frac{\partial^2 T}{\partial z^2} = 0, \text{(Laplace's equation)}. \tag{1.6}$$

In Table 1.1 some examples of representative thermal conductivity values for different minerals, rocks, and fluids are displayed.

Material	Thermal conductivity (W/mK)
Quartz crystal	9.10
Quartz glass	1.27
Granite	1.72-3.85
Calcium carbonate	3.80
Marble	2.08-2.94
Limestone	2.22
Ice	2.22
Sandstone	2.00
Dolomite	1.72
Slate	1.49
Mica	0.59
Steel	16-43
Concrete	0.10-1.70
Water	0.61
Air	0.03

Table 1.1: Thermal conductivity values for different minerals, rocks, and fluids. (T. Anikó, 2014)

Since the physical model, object of this work, in absence of filtration motion, is assumed to be characterized by an axisymmetric behavior in

respect to the probe axis, it becomes useful to consider Laplace's equation (equation (1.6)) in cylindrical coordinates (Figure 1.5), as follows:

$$\frac{d^2T}{dr^2} + \frac{1}{r} \cdot \frac{dT}{dr} = 0.$$

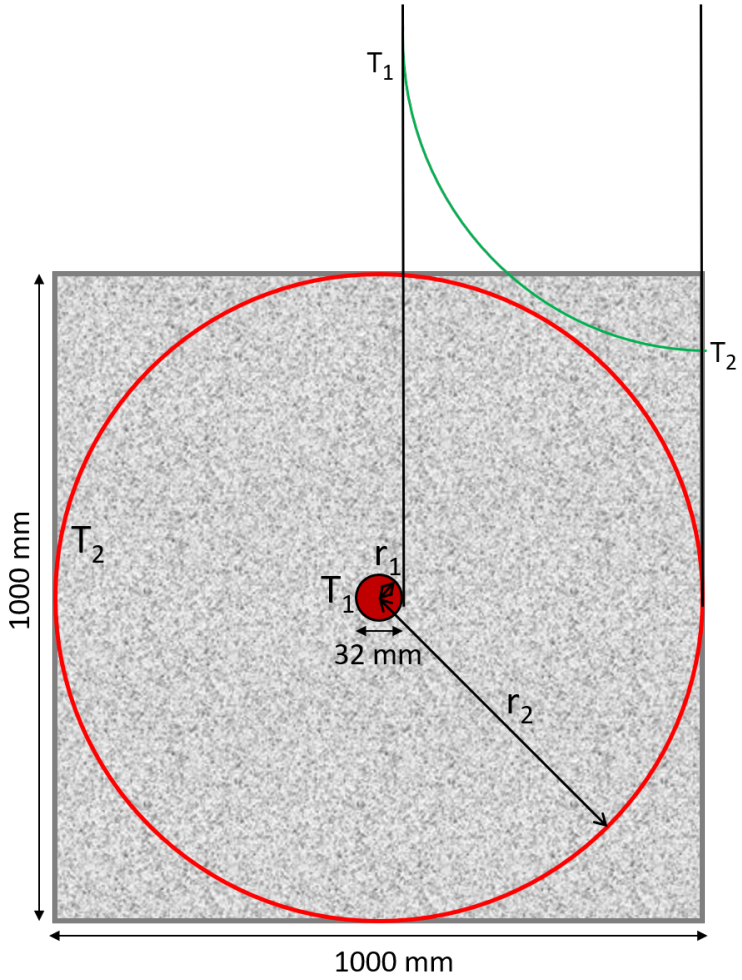

Figure 1.5: Conduction in cylindrical coordinates, the streaked area represents the control volume while the inner circle represents the thermal probe.

The solution of the differential equation is:

$$T = C_1 \cdot \log r + C_2$$

and specializing the solution considering the boundary conditions of Figure 1.5:

$$T = T_1 - \frac{T_1 - T_2}{\ln \frac{r_2}{r_1}} \cdot \ln \frac{r}{r_1} \tag{1.7}$$

where T is the temperature to be calculated, T_1 is the temperature at distance r_1 from the probe, T_2 is the temperature at distance r_2 from the probe and r is the distance from the probe at which T is calculated.

The energy flux becomes:

$$q = -\lambda \cdot A \cdot \frac{dT}{dr} = -\lambda \cdot 2\pi r \cdot l \cdot \frac{dT}{dr}$$

$$q = \frac{T_1 - T_2}{\frac{1}{2\pi \cdot l \cdot \lambda} \ln \frac{r_2}{r_1}} \tag{1.8}$$

It can be concluded that the thermal resistance to the heat flux q, the denominator of the equation (1.8), grows with a logarithmic law of the ratio between external radius and internal radius of the material inside the control volume.

Chapter 2

The Experimental Apparatus

2.1 Supporting Structure

The supporting structure of the experimental apparatus is shown in Figure 2.1. It's approximately 2 m high, 1.5 m long, 1.1 m wide and its mass is roughly 300 kg. The materials used are aluminum for the load-bearing structure, the piers of which have a square section of 6 cm side, and steel for the supporting elements of the side walls (steel bars) which have a rectangular section of 6 cm x 2 cm.

The 2 mm thick perforated walls, also made of steel, are used for the internal support of the granular material and the total area of their holes is approximately the 50% of the total surface, so allowing the filtration fluid to flow inlet and outlet the volume (Figure 2.1a).

At the bottom and the top the model is isolated by 6 cm thick polyethylene

slabs. A 20 mm thick opaque PVC slab constitutes the bottom of the apparatus whereas the side walls are made of 10 mm thick transparent PVC panels. Furthermore in Figure 2.1b the distributors of the filtration fluid are shown, made with micro-pitted PVC pipes, and the flow rectifiers, made of polycarbonate honeycomb sheets.

The upstream and downstream closure steel walls of the model and the output tanks of the filtration fluid are displayed in Figure 2.1c. To stabilize the piezometric elevation of the filtration fluid in and out the model both tanks are implemented with spillways. The maximum piezometric gradient attainable is about 0.25 m/m. In Figure 2.1c it is also visible the copper pipe which acts as heat exchanger, the copper was chosen due to its higher thermal power per unit length than Polythene (PE) that is the typical material used for the manufacturing of thermal probes. This choice leads to an amplification of the effects of the energy exchange between the probe and the surrounding material. The pipe has an internal diameter of 28 mm , a thickness of 2 mm and a length inside the apparatus of 0.95 m.

Figure 2.2 displays the apparatus realized as explained. The aluminum piers are implemented with height-adjustable supports which allow to level the structure.

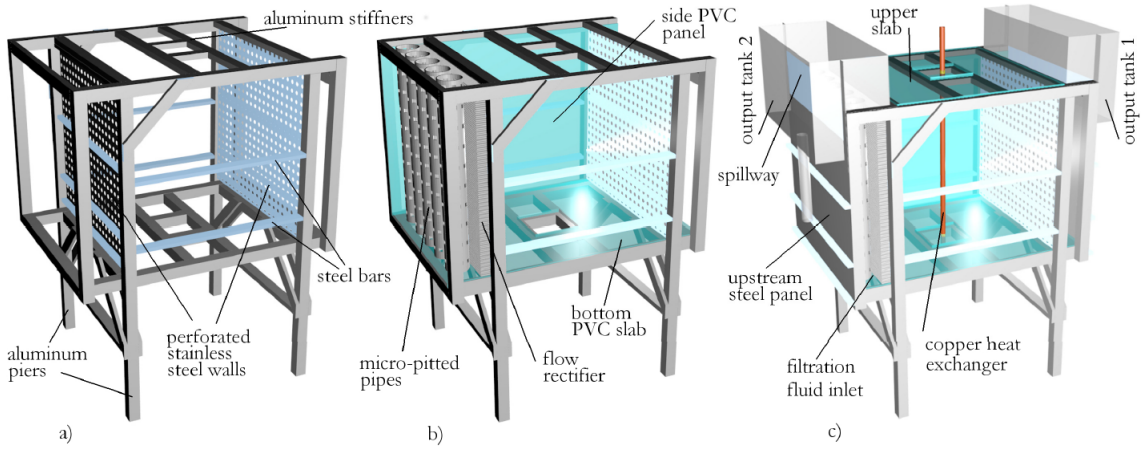

Figure 2.1: The bearing structure of the experimental apparatus. The materials used are aluminum, steel and PVC.

Figure 2.2: a) The experimental apparatus in test configuration. The insulated circuit of the copper heat exchanger is visible; b) A view from the top of the filtration fluid inlet tank with the micro-pitted pipes; c) The perforated stainless steel wall; d) A detail of the flow rectifier located between the micro-pitted pipes and the perforated wall.

2.2 Hydraulic Circuits

The physical model in object has been designed with two hydraulic circuits, one for the cold fluid (HCC) and one for the hot fluid (HCH), and each one can be plugged into the probe circuit or into the filtration fluid circuit. In Figure 2.3 are schematized the connection points of the circuit of the thermal probe and of the filtration fluid related to the experimental apparatus. The fluid from the probe circuit flows into the upper part of the copper probe (inputCS) and returns to its circuit at the lower end of the probe (outputCS). The fluid from the filtration fluid circuit is inserted in the lower part of the loading tank (inputCF). To ensure the flow stability through the porous medium of the model two spillways are placed in the loading tank and in the discharge tank, respectively, thus two discharges of the filtration circuits are in place: one from the discharge tank (outputCF1) and one from the loading tank (outputCF2). The circuits are designed so that a steady flow rate with constant temperature at the model inputs is ensured.

2.2.1 Thermal Power, Flow Rate and Flow Regime in the Hydraulic Circuits

The range of variability of the flow rate in the hydraulic circuits is a function of the temperature variation that occurs in the fluid after it covers the entire circuit. A machine of adequate power must be used to restore this temperature difference, in heating or cooling. The dependence between the

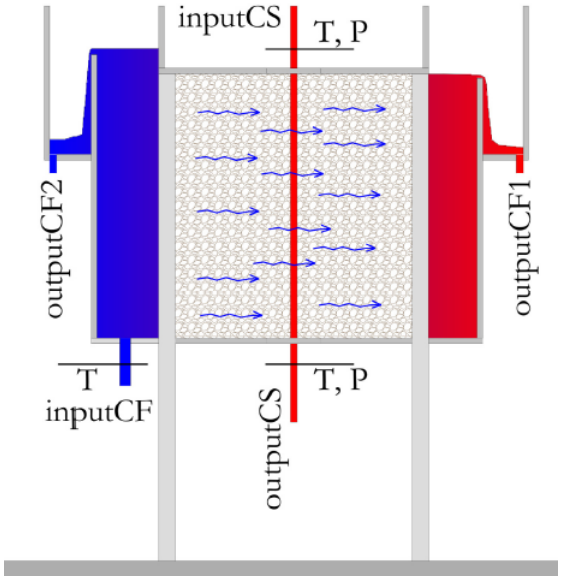

Figure 2.3: Scheme of the experimental apparatus with indication of input and output points of the cold and hot hydraulic circuit.

power of the thermal machine and the flow rate that can be managed if the temperature variation range in the circuit is between 1°C and 4°C is shown in Figure 2.4. In case of using a $4kW$ power machine, the obtainable flow rate varies between $0.24\frac{l}{s}$ with a 4°C temperature variation in the circuit and $0.96\frac{l}{s}$ with a 1°C temperature variation in the circuit.

Figure 2.5 shows the dependence between the flow rate in the probe circuit and the temperature of the fluid (water) when the diameter of the probe tube varies. On the left graph is presented the situation at the limit of laminar flow (Reynolds number, Re, is 2000). The maximum flow rate of $\backsim 0.101\ \frac{l}{s}$ is obtained with the maximum diameter considered of 35 mm at low temperatures. This flow rate is easily achieved with the designed

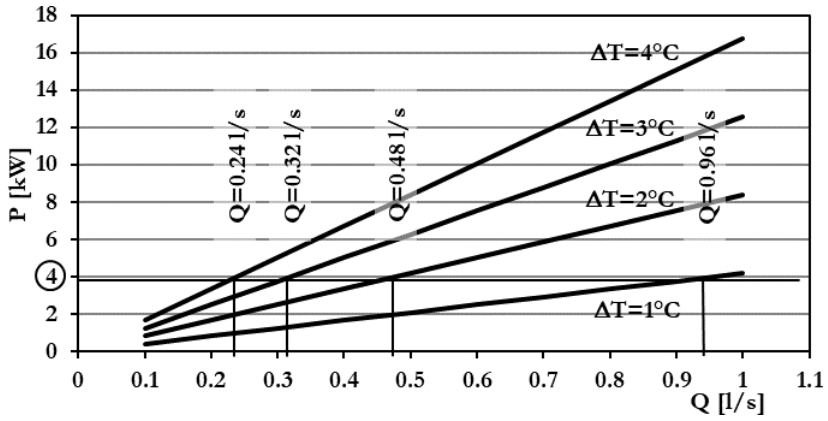

Figure 2.4: Power of the thermal machine vs flow rate when the temperature in the probe circuit fluid varies between 1°C and 4°C.

power of the circuit. On the right graph is presented the situation in case the Re in the probe circuit is 20000. At temperatures slightly above 0°C and considering the maximum diameter (35 mm) the flow rate is 0.9 $\frac{l}{s}$ which is close to the maximum value obtainable from the probe circuit. The Re values considered are close to the maximums technologically adopted. The limits of the filtration fluid velocity in the porous medium are calculated as a function of the maximum obtainable flow rate (between 0.25 $\frac{l}{s}$ and 1 $\frac{l}{s}$), the maximum piezometric gradient ($\backsim 0.2$ $\frac{m}{m}$) and the filtration area ($\backsim 1$ m^2). The velocity varies between $2.7{\cdot}10^{-4}$ $\frac{m}{s}$ and $1.2{\cdot}10^{-3}$ $\frac{m}{s}$. The hydraulic conductivity, in the case of Darcy flow, ranges between $1.4{\cdot}10^{-3}$ $\frac{m}{s}$ and $5.5{\cdot}10^{-3}$ $\frac{m}{s}$, which is the case of clean sand, sand and gravel.

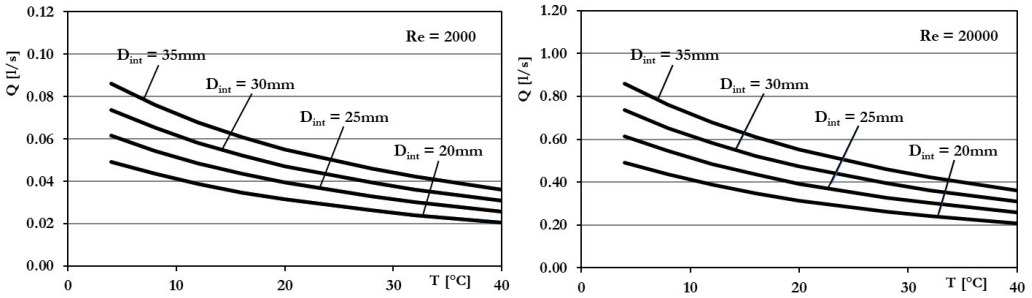

Figure 2.5: Flow rate vs temperature of the thermal probe circuit for two Reynolds numbers and different probe diameters.

2.3 Temperature Sensors

To measure the temperature inside the volume, Resistance Temperature Detectors (RTDs) are used (Figure 2.6), specifically PT100 RTDs with three-wire connections. Their sensitivity is less than 0.1 °C and the calibration curve is very close to linearity. The mayor downside is that their response time is not particularly short and varies depending on the material used for the protection of the sensor. The protection used during the test is made of a water permeable metal sock. The resulting response time of 2-3 seconds is considered compatible with the temperature variation times that occur in the physical model.

The PT100 sensors measures the temperature of the fluid in the copper probe (at both up and down ends), of the filtration fluid entering the control volume, of the environment and in 24 positions inside the control volume. The temperature sensors layout is shown in Figure 2.7. The RTDs are placed on glass rods at different heights from the bottom of the control volume.

Figure 2.6: PT100 Resistance Temperature Detector with the metal sock protection used in the test.

The rods are positioned at different distances from the copper probe. In the case of absence of groundwater flow, like in the configuration of the test, the temperature distribution should be axis-symmetric around the thermal probe vertical axis. To verify this hypothesis the RTDs placed to the right of the probe (Figure 2.7) are in a symmetrical position with respect to the ones on the left side. A maximum of 42 analogical channels can be served by the acquisition system in use.

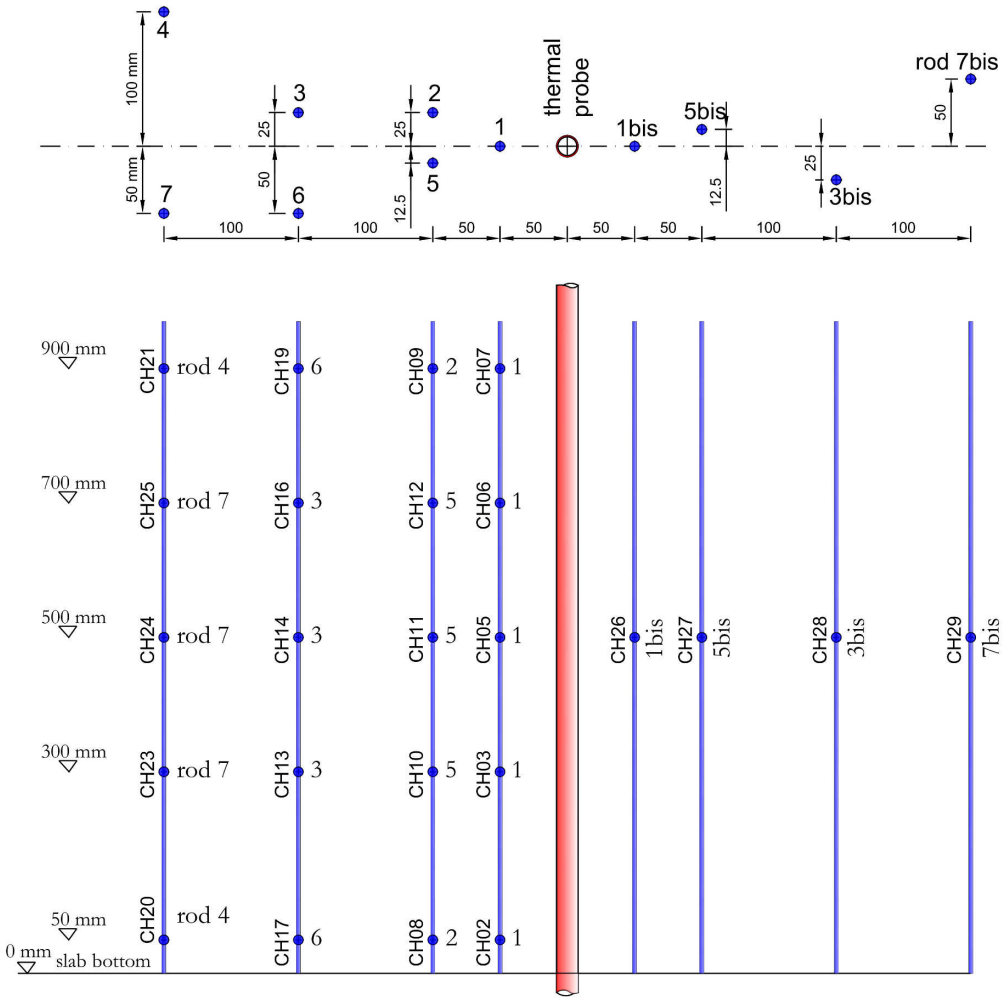

Figure 2.7: Above: planimetric position of the rods supporting the RTDs inside the control volume; below: rod and elevation with respect to the bottom of the control volume of each RTD.

Chapter 3

Test Configuration

The experimental configuration adopted for the test is characterized by absence of water and the control volume filled up with dry granular material, specifically *"Risetta del Brenta"* (Figure 3.1), (which literally means small rice from the Brenta river) bought from the "Ghiaie Fontaniva" company of Fontaniva (PD). That is a sandy-gravelly material taken from the bed of the Brenta river nearby Padova. The grain size distribution of the granular material has been evaluated on two samples at the Geotechnical Engineering Laboratory of the University of Padua. The results are displayed in Table 3.1 and Figure 3.2. The material is classified as fine-medium coarse gravel. By letting the granular material fall into still water in the control volume it was possible to measure the excess water volume (0.505 m^3), knowing the mass of the *Risetta del Brenta* put into the model (1365.17 kg) an estimation of both the average density of the granular material (2700 $\frac{kg}{m^3}$) and its porosity

(0.43) has been calculated.

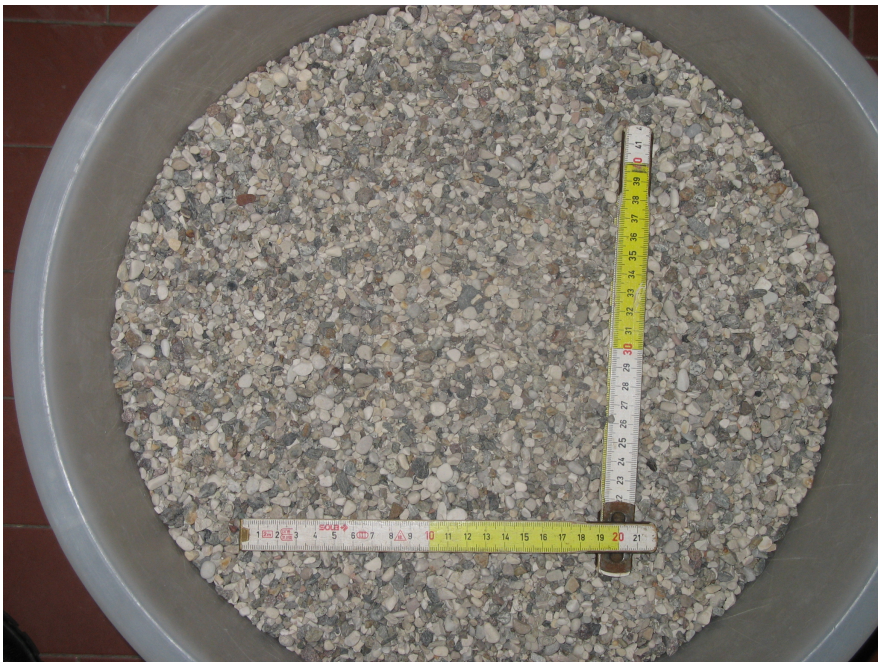

Figure 3.1: *Risetta del Brenta*, the granular material adopted in the test.

The thermal conductivity of the dry granular material has been estimated as 0.5 $\frac{W}{mK}$ through tests performed at the Geoscience Department.
The environment temperature is 20 °C while the temperature of the water flowing into the thermal probe is around 40 °C.
The flow rate inside the probe is 0.421-0.422 $\frac{l}{s}$ ($\backsimeq$25.3 $\frac{l}{min}$).

In Table 3.2 are presented the acquisition channels related to each PT100 sensor positioned inside the control volume, at both ends of the copper probe and outside the control volume.

GRANULOMETRIC ANALYSIS

SAMPLE 1					SAMPLE 2				
Vaglio n.	D Vaglio	Peso netto (g)	% Trattenuto	% Passante	Vaglio n.	D Vaglio	Peso netto (g)	% Trattenuto	% Passante
4"	101.6		0.00	100.00	4"	101.6		0.00	100.00
3"	76.2		0.00	100.00	3"	76.2		0.00	100.00
2"	50.8		0.00	100.00	2"	50.8		0.00	100.00
1" 1/2	38.1		0.00	100.00	1" 1/2	38.1		0.00	100.00
1"	25.4		0.00	100.00	1"	25.4		0.00	100.00
3/4"	19.1		0.00	100.00	3/4"	19.1		0.00	100.00
1/2"	12.7		0.00	100.00	1/2"	12.7		0.00	100.00
3/8"	9.52	8.4	0.41	99.59	3/8"	9.52		0.00	100.00
4	4.76	929.2	45.26	54.33	4	4.76	902.8	32.36	67.64
10	2	1082.1	52.71	1.62	10	2	1797.3	64.42	3.22
20	0.84	22.5	1.10	0.53	20	0.84	65.7	2.36	0.86
40	0.42	1.3	0.06	0.46	40	0.42		0.00	0.86
60	0.25		0.00	0.46	60	0.25		0.00	0.86
80	0.177		0.00	0.46	80	0.177		0.00	0.86
140	0.105		0.00	0.46	140	0.105		0.00	0.86
200	0.074	6.2	0.30	0.16	200	0.074	23.4	0.84	0.02

Table 3.1: Granulometric distribution of two samples of *Risetta del Brenta* used in the test.

acquisition channel	internal external sound	rod number	elevation from the bottom [mm]	acquisition channel	internal external sound	rod number	elevation from the bottom [mm]	acquisition channel	internal external sound	rod number	elevation from the bottom [mm]
CH00	external			CH14	internal	3	+500	CH28	internal	3bis	+500
CH01	external			CH15	external			CH29	internal	7bis	+500
CH02	internal	1	+50	CH16	internal	3	+700	CH30	room	---	---
CH03	internal	1	+300	CH17	internal	6	+50	CH31	not used	---	---
CH04	external			CH18	external			CH32	not used	---	---
CH05	internal	1	+500	CH19	internal	6	+900	CH33	discharge	---	---
CH06	internal	1	+700	CH20	internal	4	+50	CH34	not used	---	---
CH07	internal	1	+900	CH21	internal	4	+900	CH35	not used	---	---
CH08	internal	2	+50	CH22	external			CH36	not used	---	---
CH09	internal	2	+900	CH23	internal	7	+300	CH37	not used	---	---
CH10	internal	5	+300	CH24	internal	7	+500	CH38	not used	---	---
CH11	internal	5	+500	CH25	internal	7	+700	CH39	not used	---	---
CH12	internal	5	+700	CH26	internal	1bis	+500	CH40	not used	---	---
CH13	internal	3	+300	CH27	internal	5bis	+500	CH41	not used	---	---

Table 3.2: The acquisition channels of the RTDs used in the control volume (internal), in the thermal probe (external), in the surrounding environment (room) and the one connected to the discharge metre (discharge).

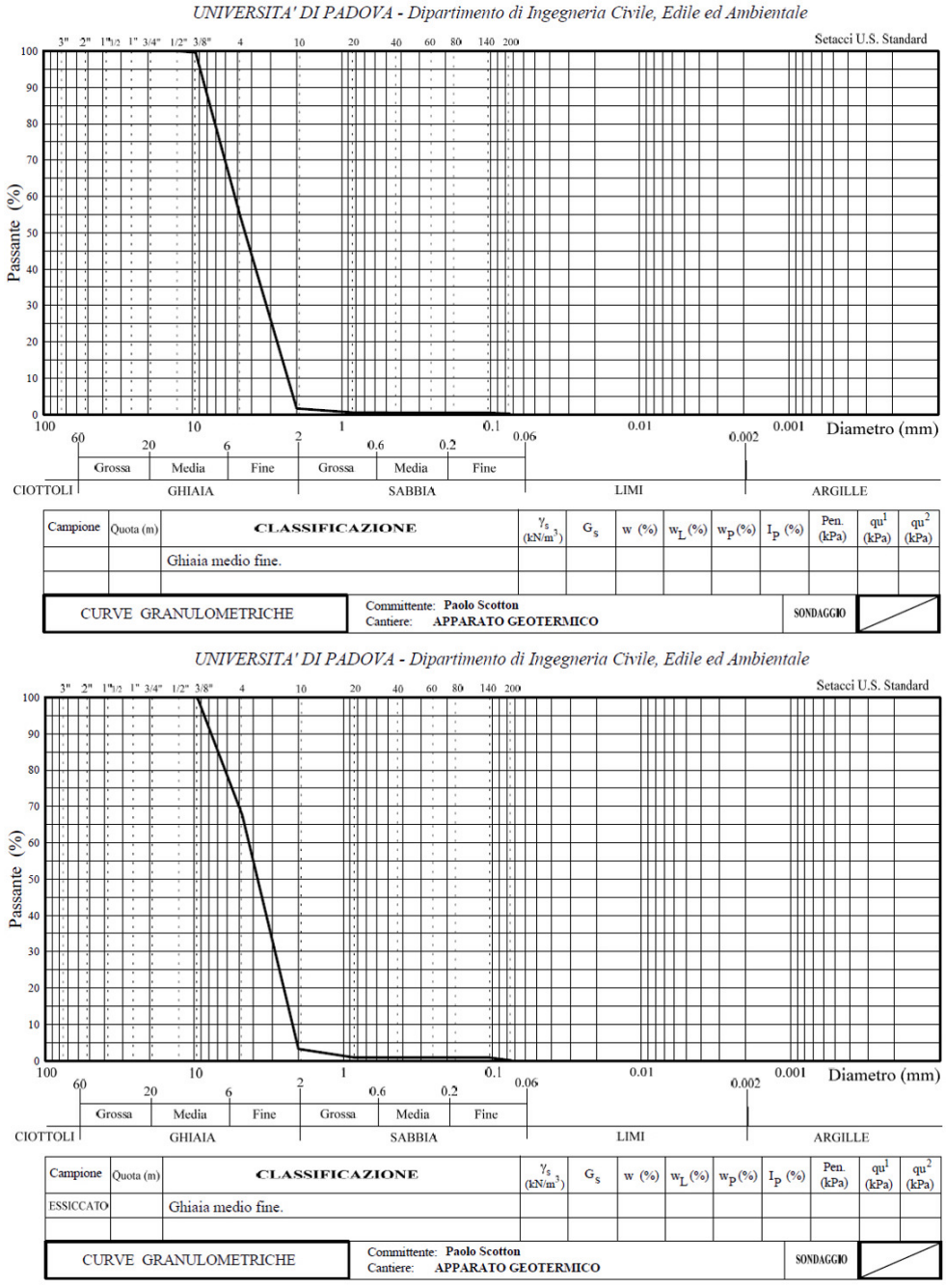

Figure 3.2: Granulometric curve of two samples of *Risetta del Brenta* used in the test. Data from Table 3.1.

3.1 Acquisition System

The acquisition system (logger, Figure 3.3) has been developed by the *TecnoPenta* Company of Teolo (PD).

It collects the data in a SD card inside of a file named DATA_xx.TXT where xx stands for a counter which ensure no accidental files overwriting. Each file contains a synthetic heading that illustrates at the first row the serial number of the logger and the configuration number (in this case: LOGGER001), at the second row the date and time of beginning of the acquisition, at the third row the tension value of the battery in Volt and in the fourth row the notehead of the channels columns. The following rows are used to display the readings in mA (milliAmps) and the first column contains a seconds counter for each row starting from the beginning of the acquisition process.

Figure 3.3: The acquisition system endowed with 42 channels for the acquisition of data from the experimental apparatus.

Chapter 4

Data Acquisition and Processing

4.1 Acquired Data

The graph in Figure 4.1 shows the temperature of each acquisition channel related to time in seconds.

The upper line refers to the temperature measured inside the thermal probe. The fluctuations are due to the periodic activation of the thermal resistance inside the boiler that permits to maintain the temperature of the fluid inside the probe almost stable.

The bottom line refers to the environment temperature. Again there are fluctuations that depend on the periodic activation of the room convector and that shows different day and night cycles.

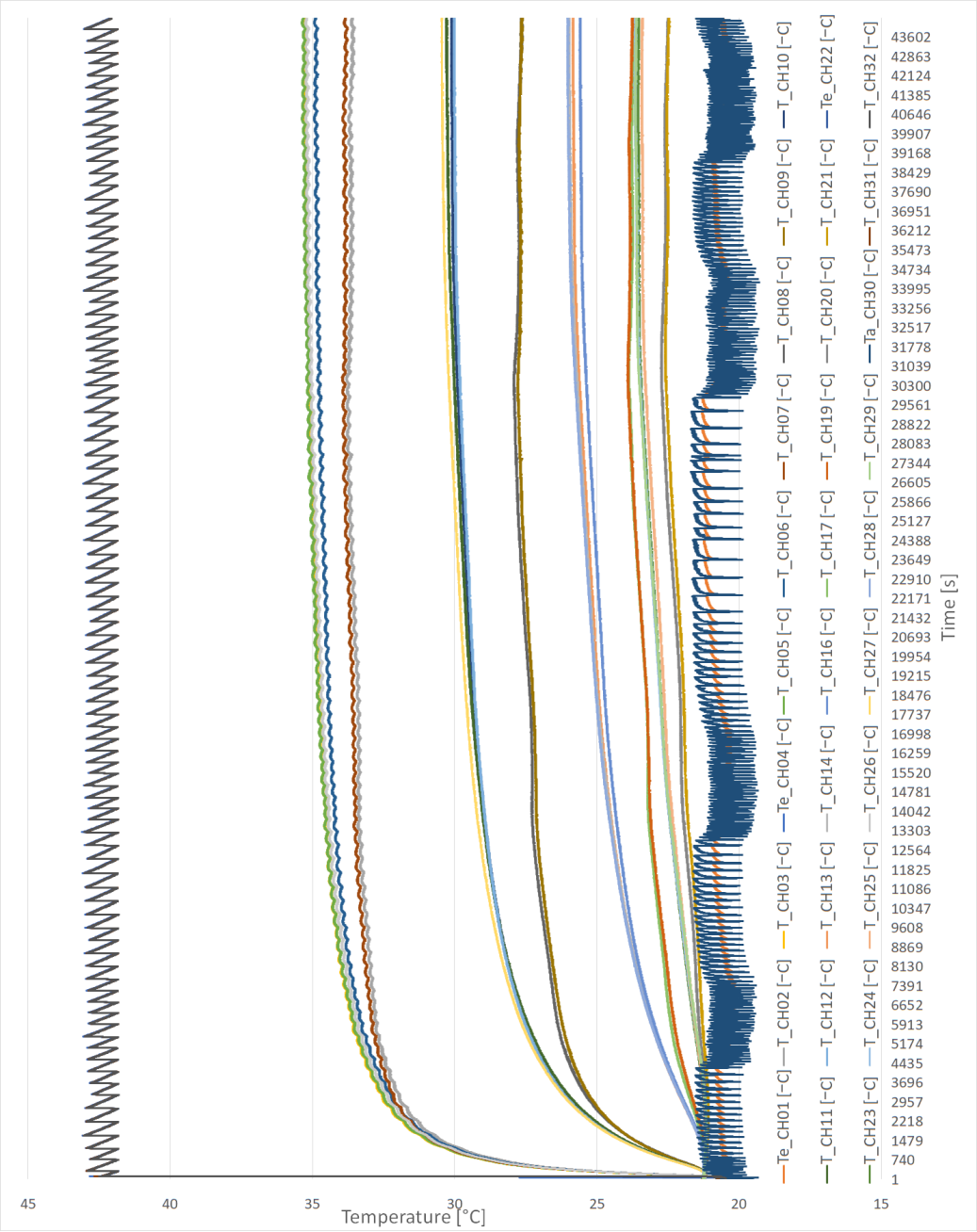

Figure 4.1: Data from each acquisition channel. In Table 3.2 are displayed the relations between the acquisition channels and the rods inside the control volume.

4.2 Symmetrical Behavior

In order to verify the axial-symmetrical behaviour of the thermal energy propagation, data collected by the temperature sensors in axial symmetric position with respect to the thermal probe (Figure 2.7) are considered.

In Figure 4.2 the data from couples of axisymmetric temperature sensors are displayed to appreciate the overlap between them, which is remarkable.

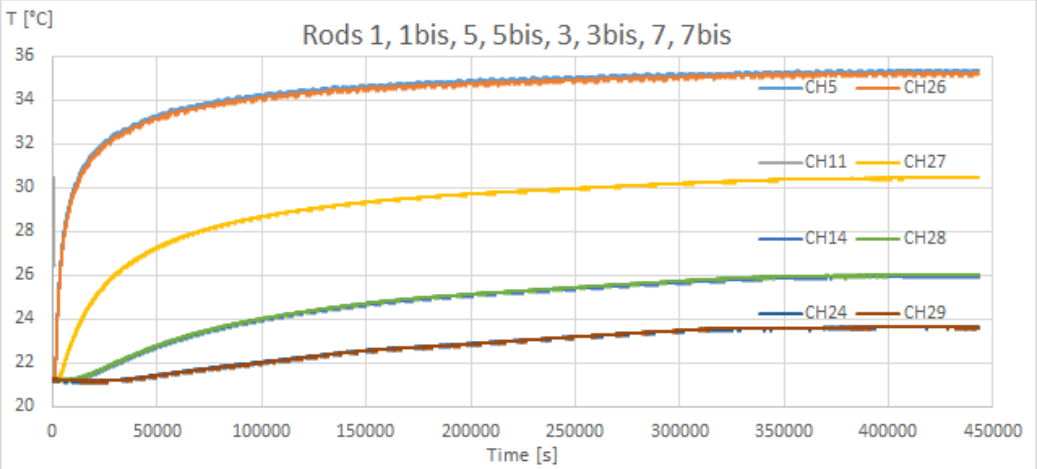

Figure 4.2: Data from axisymmetric temperature sensors with respect to the thermal probe, respectively in order from nearest to farthest from the probe: 1-1bis, 5-5bis, 3-3bis and 7-7bis.

In order to deeply understand and quantify data matching between axisymmetric sensors some more graphs have been made placing the temperature measured by couples of axisymmetric sensors on the two axis (Figure 4.3). Theoretically, assuming an axisymmetric behavior, data in Figure 4.3 should dispose according to a straight line, passing through the origin, at 45 degrees with respect to the axes of the reference system. One can identify this behav-

ior in the graphs.

In all cases (for all distances from the probe) the linear regression gives values of the determination coefficient which are very near to 1, and the intersection of the straight line with the y-axis is very near to 0.

Let's now consider the legitimacy of the axisymmetric behavior hypothesis with respect to the thermal probe axis. Figures 4.2 and 4.3 confirm this behavior even if the data don't perfectly overlap, like they should do in theory. The small divergences in values of data from axisymmetric sensors, which point out small temperature differences, may be caused by many factors that affect very little the symmetry hypothesis such as anisotropy of the porous medium derived from the material deposition method adopted and from the presence of distinct minerals that can be in various ratios between them in each grain. Another cause could be the presence of discontinuities between the grains, that locally affects the physical properties but may also have an effect on fluid (air in the case of the test presented in this work) convection in the control volume, creating channels of different size and form for air to flow in. Instrumental errors can affect the results as well.

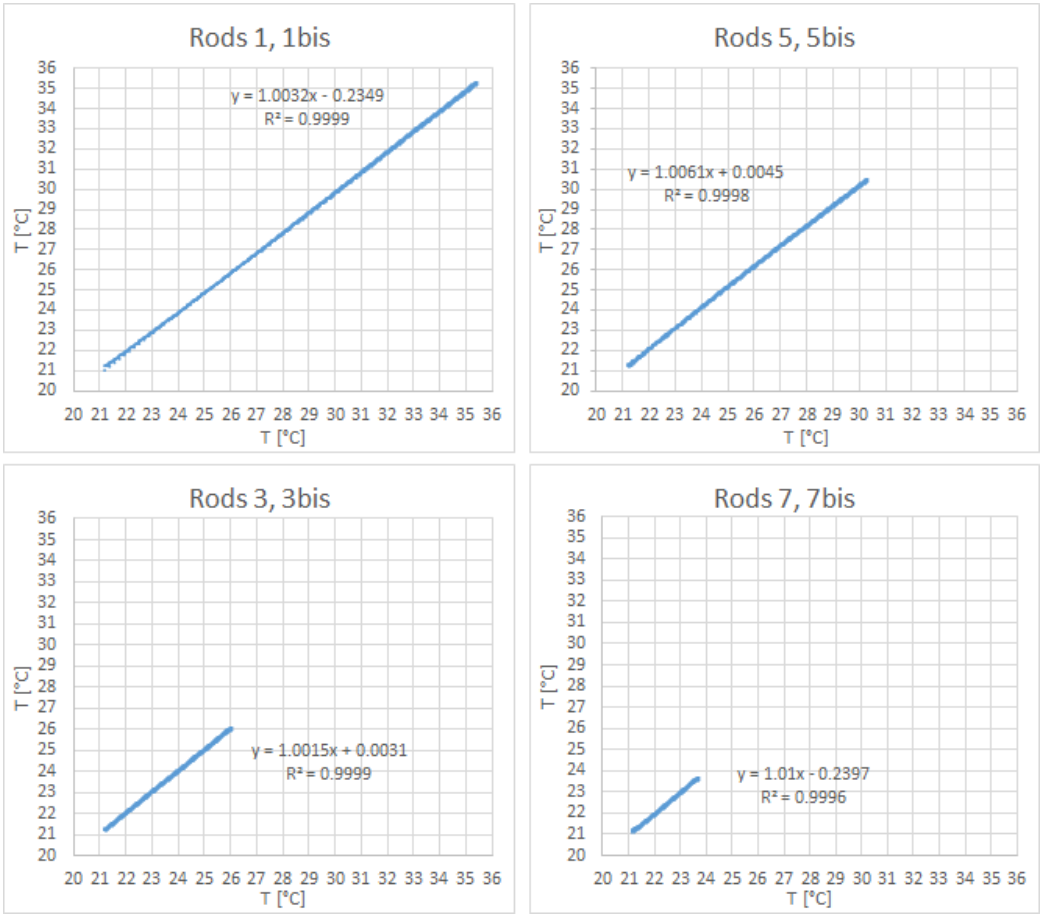

Figure 4.3: Comparison between the data from axisymmetric temperature sensors with respect to the thermal probe, respectively in order from nearest to farthest from the probe: 1-1bis, 5-5bis, 3-3bis and 7-7bis.

4.3 Data Processing

The test configuration described in Chapter 3 leads to a very small temperature difference between inlet and outlet temperature gauges of the thermal probe (see Figure 2.3). This is caused by the intergranular fluid, the air, that acts as a thermal insulation agent, reducing the energy exchange between the thermal probe and the surrounding volume.
The temperature difference is of the same order of magnitude of the sensitivity of the temperature sensors (0.05°C), so that it is not reasonable to apply the procedures illustrated in § 1.2 to evaluate the power of the probe. Nevertheless, the evolution in time of the energy acquired by the volume around the probe is quite well defined by the temperature field measured by the thermal sounds distributed inside the granular volume.

4.3.1 Comparison With Fourier's Heat Conduction Law

The Figures 4.4, 4.5, 4.6, 4.7, 4.8, 4.9, 4.10, 4.11, 4.12, 4.13, 4.14, 4.15, 4.16, 4.17, 4.18, 4.19, 4.20, 4.21, 4.22, 4.23, 4.24, 4.25, 4.26, 4.27, 4.28, 4.29, 4.30, 4.31, 4.32 and 4.33 present the temperature trend at 50, 300, 500, 700 and 900 mm height from the bottom of the control volume at different times. Each graph displays the measured temperature trend (blue curve) and the theoretical temperature trend (orange curve) calculated, in steady state conditions, through Fourier's conduction equation derived in cylindrical coordinates (equation (1.7)).

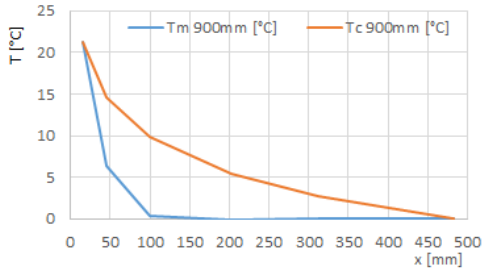

Figure 4.4: Temperature trends at 900 mm from the bottom after 5.000 seconds, measured (blue) and calculated (orange).

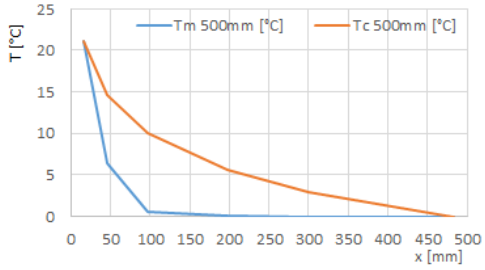

Figure 4.5: Temperature trends at 500 mm from the bottom after 5.000 seconds, measured (blue) and calculated (orange).

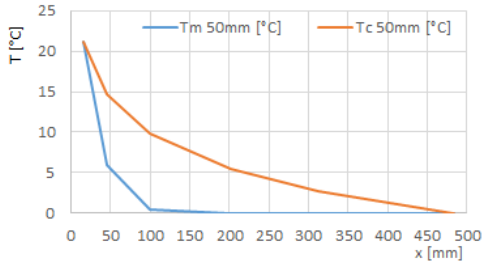

Figure 4.6: Temperature trends at 50 mm from the bottom after 5.000 seconds, measured (blue) and calculated (orange).

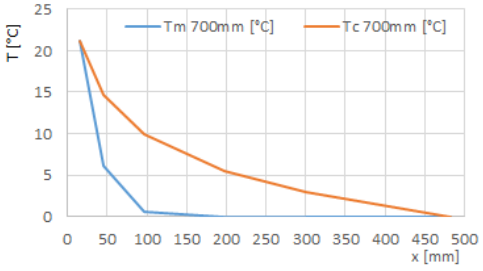

Figure 4.7: Temperature trends at 700 mm from the bottom after 5.000 seconds, measured (blue) and calculated (orange).

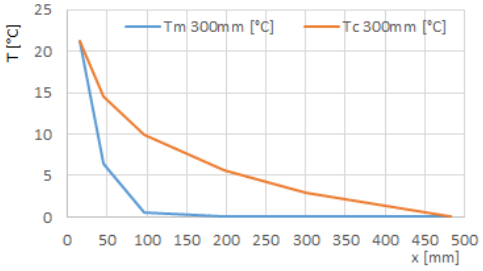

Figure 4.8: Temperature trends at 300 mm from the bottom after 5.000 seconds, measured (blue) and calculated (orange).

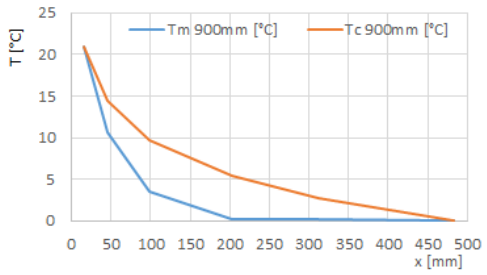

Figure 4.9: Temperature trends at 900 mm from the bottom after 25.000 seconds, measured (blue) and calculated (orange).

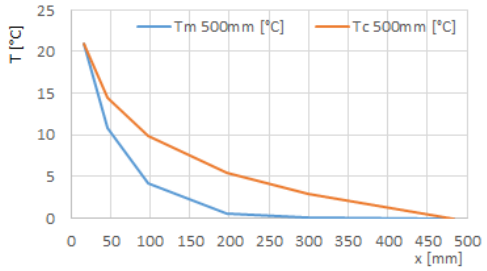

Figure 4.10: Temperature trends at 500 mm from the bottom after 25.000 seconds, measured (blue) and calculated (orange).

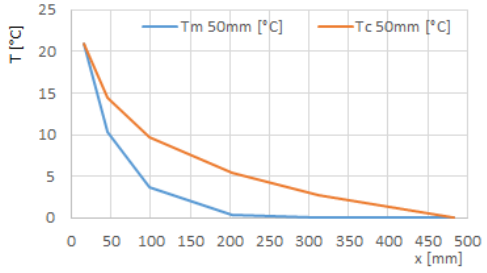

Figure 4.11: Temperature trends at 50 mm from the bottom after 25.000 seconds, measured (blue) and calculated (orange).

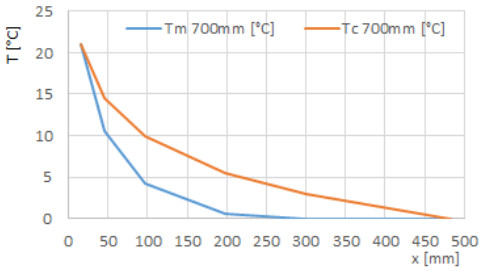

Figure 4.12: Temperature trends at 700 mm from the bottom after 25.000 seconds, measured (blue) and calculated (orange).

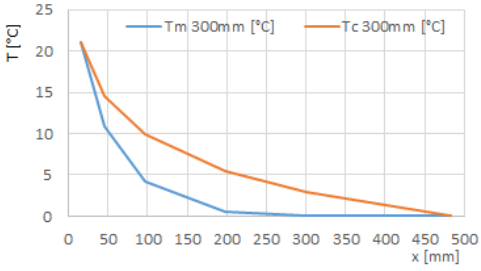

Figure 4.13: Temperature trends at 300 mm from the bottom after 25.000 seconds, measured (blue) and calculated (orange).

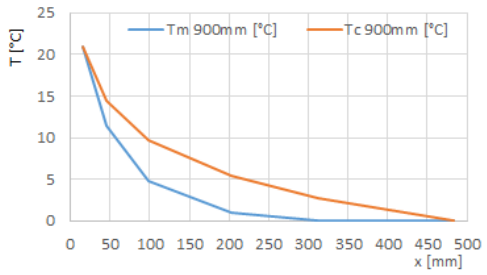

Figure 4.14: Temperature trends at 900 mm from the bottom after 50.000 seconds, measured (blue) and calculated (orange).

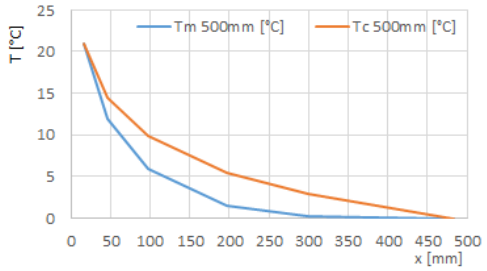

Figure 4.15: Temperature trends at 500 mm from the bottom after 50.000 seconds, measured (blue) and calculated (orange).

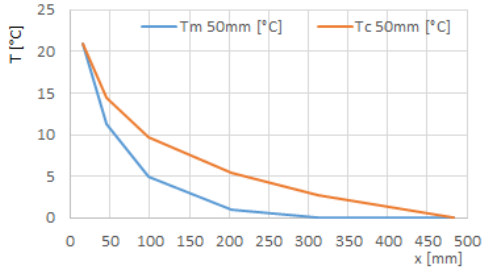

Figure 4.16: Temperature trends at 50 mm from the bottom after 50.000 seconds, measured (blue) and calculated (orange).

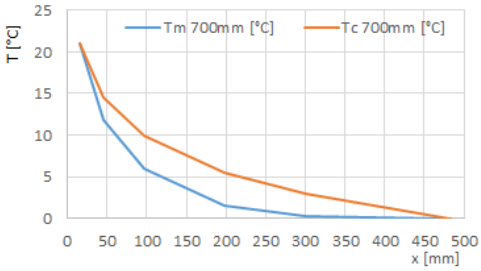

Figure 4.17: Temperature trends at 700 mm from the bottom after 50.000 seconds, measured (blue) and calculated (orange).

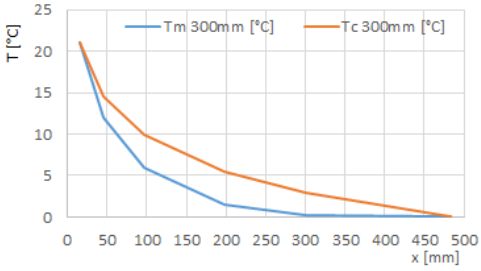

Figure 4.18: Temperature trends at 300 mm from the bottom after 50.000 seconds, measured (blue) and calculated (orange).

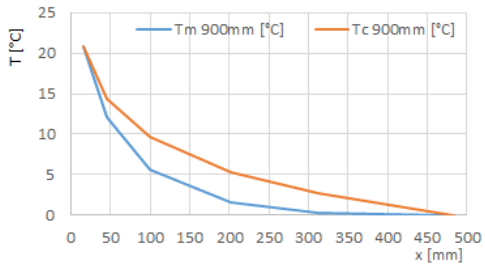

Figure 4.19: Temperature trends at 900 mm from the bottom after 100.000 seconds, measured (blue) and calculated (orange).

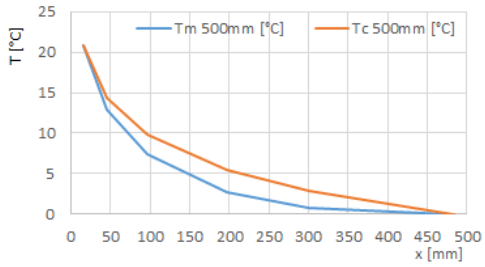

Figure 4.20: Temperature trends at 500 mm from the bottom after 100.000 seconds, measured (blue) and calculated (orange).

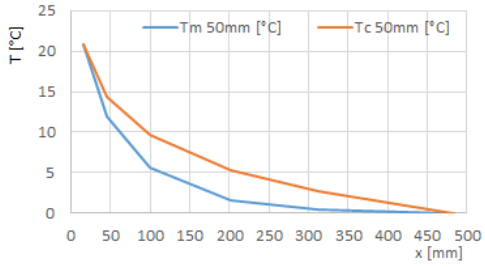

Figure 4.21: Temperature trends at 50 mm from the bottom after 100.000 seconds, measured (blue) and calculated (orange).

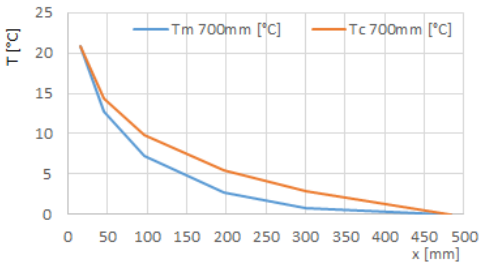

Figure 4.22: Temperature trends at 700 mm from the bottom after 100.000 seconds, measured (blue) and calculated (orange).

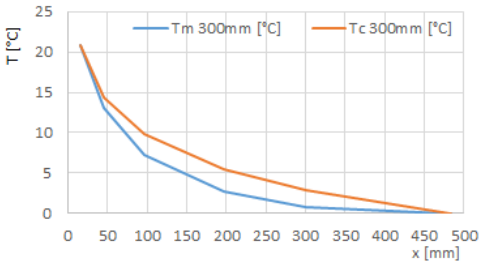

Figure 4.23: Temperature trends at 300 mm from the bottom after 100.000 seconds, measured (blue) and calculated (orange).

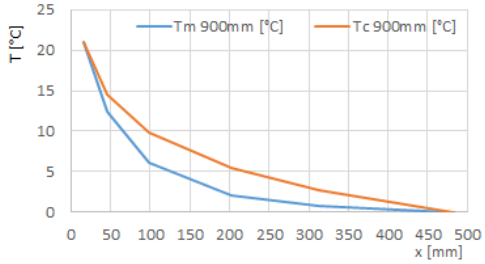

Figure 4.24: Temperature trends at 900 mm above the bottom after 200.000 seconds, measured (blue) and calculated (orange).

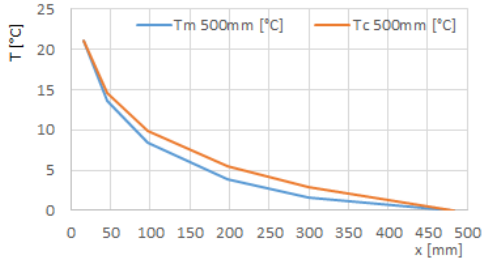

Figure 4.25: Temperature trends at 500 mm above the bottom after 200.000 seconds, measured (blue) and calculated (orange).

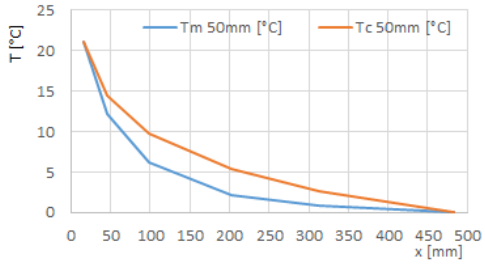

Figure 4.26: Temperature trends at 50 mm above the bottom after 200.000 seconds, measured (blue) and calculated (orange).

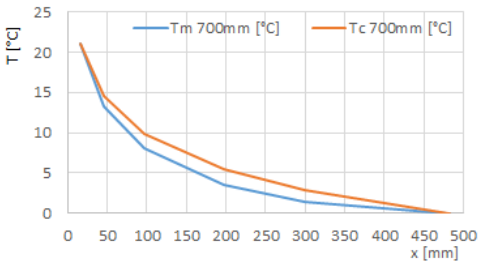

Figure 4.27: Temperature trends at 700 mm above the bottom after 200.000 seconds, measured (blue) and calculated (orange).

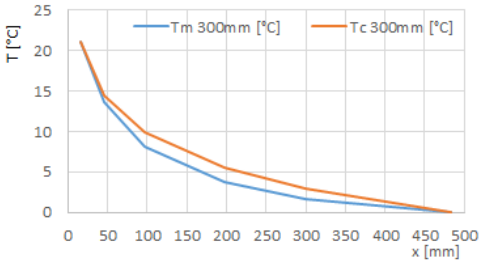

Figure 4.28: Temperature trends at 300 mm above the bottom after 200.000 seconds, measured (blue) and calculated (orange).

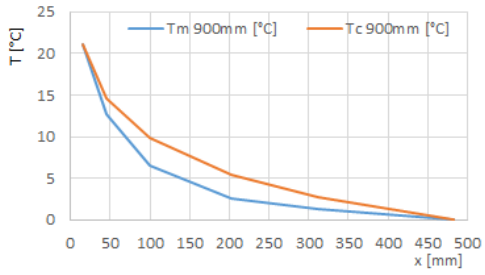

Figure 4.29: Temperature trends at 900 mm above the bottom after 400.000 seconds, measured (blue) and calculated (orange).

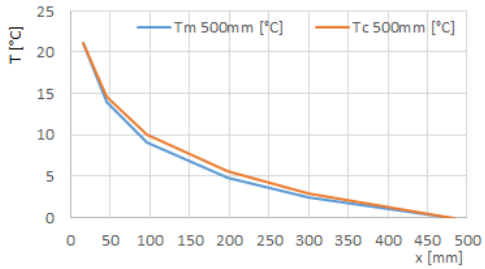

Figure 4.30: Temperature trends at 500 mm above the bottom after 400.000 seconds, measured (blue) and calculated (orange).

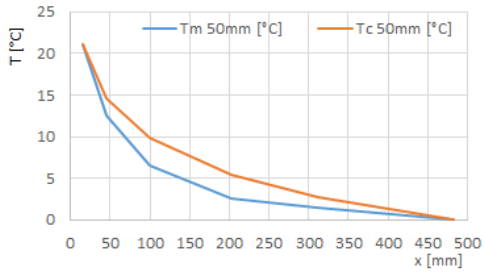

Figure 4.31: Temperature trends at 50 mm above the bottom after 400.000 seconds, measured (blue) and calculated (orange).

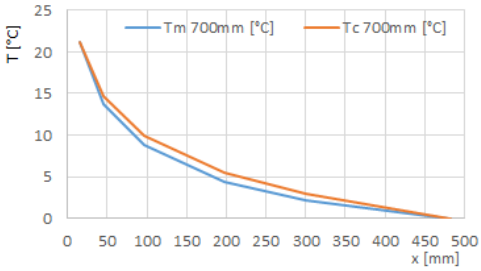

Figure 4.32: Temperature trends at 700 mm above the bottom after 400.000 seconds, measured (blue) and calculated (orange).

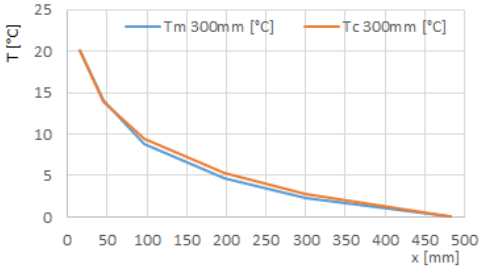

Figure 4.33: Temperature trends at 300 mm above the bottom after 400.000 seconds, measured (blue) and calculated (orange).

One can detect that the separation between the two curves decreases with time (towards steady state conditions). Another aspect to be noted is that, especially after 100000 seconds and at the same time instant, curves referred to the maximum (900 mm) and minimum (50 mm) height differ more than the curves referred to the internal height values (300 mm, 500 mm, 700 mm) from the theoretical solution curve.

To quantify the difference between measured and theoretical regime values, the following R parameter has been calculated:

$$R = \sqrt{\frac{\sum_{i=1}^{4}(T_m - T_t)^2}{4}}$$

where T_m is the measured temperature and T_t is the theoretical regime temperature, according to the heat conduction theory (Section 1.3).

The obtained R values are displayed in Table 4.1 where are also shown the mean values of R for each height considered and for each time considered, in addition to this the mean of the internal height values for each time considered has been calculated.

A comparison between the R values for each time considered is reported by Figure 4.34.

Figure 4.34 shows the trend of R values for each time considered. Initially

R [°C]	height [mm]						
time [s]	**50**	**300**	**500**	**700**	**900**	**mean**	**internal values mean**
5000	7.1	7.0	7.0	7.1	7.0	7.0	7.0
25000	4.6	4.4	4.4	4.5	4.6	4.5	4.4
50000	3.8	3.4	3.4	3.4	3.9	3.6	3.4
100000	3.2	2.2	2.2	2.3	3.3	2.6	2.3
200000	2.8	1.4	1.4	1.6	2.8	2.0	1.5
400000	2.5	0.5	0.7	1.0	2.5	1.4	0.8
mean	4.0	3.2	3.2	3.3	4.0		

Table 4.1: R values between measured and calculated temperature for each time and height considered. Mean values for each height considered. Mean values for each time considered and mean of the internal height values (300mm, 500mm and 700mm) for each time considered.

the values of R parameters are very similar for all the heights considered, then they diverge with time. At 400000 seconds (at steady state conditions) the values of R parameters referred to the maximum (900 mm) and minimum (50 mm) height are more than the double of the values of R parameters at the internal height positions (at 300 mm, 500 mm, 700 mm).

This behavior, that points out an important divergence between the theoretical steady state values and measured values referred to the maximum and minimum height, has been interpreted as a consequence of energy loss from the upper PVC slab and the lower PVC slab of the physical model.

Data referred to the internal height values are very near to the theoretical steady state values. In fact the average value of their R parameter is evidently smaller than the one of the upper (900 mm) and lower (50 mm) position (Table 4.1).

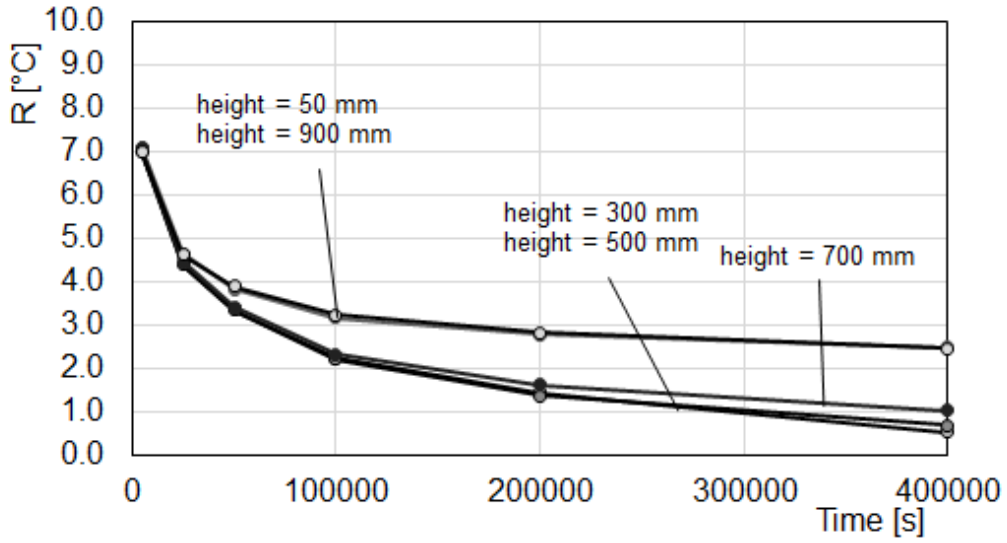

Figure 4.34: R values between measured and calculated temperature for each time and height considered.

Thus it is possible to say that the behavior of the physical model in its internal part is nearly independent of the boundary condition and can be described well by the heat conduction theory (equation (1.7)).

Estimated Power Of The Thermal Probe

Since it is not reasonable to apply the procedures illustrated in § 1.2 to evaluate the power of the probe, another road can be traveled. To calculate the heat flux per unit length of the probe (the power of the probe) in steady state conditions, it is possible to use the equation (1.8). In this case, T_1 and T_2 (Figure 1.5) are, respectively, the temperature at the surface of the probe ($r_1 = 16mm$) and the temperature at the limit of the physical model in radial

direction ($r_2 = 483mm$). The power of the thermal probe thus calculated is:

$$q = \frac{T_1 - T_2}{\frac{1}{2\pi \cdot l \cdot \lambda} \ln \frac{r_2}{r_1}} = \frac{21.16}{\frac{1}{2\pi \cdot 1 \cdot 0.5} \ln \frac{483}{16}} = 19.50 \frac{W}{m}$$

To λ a value between $0.4 - 0.5 \frac{W}{mK}$ can be assigned (Scotton et al., 2018)(Talleri, 2001). Here a value of $0.5 \frac{W}{mK}$ has been chosen.

Estimated Value Of The Thermal Probe Temperature Difference

The estimated value of the temperature difference between the probe inlet and outlet fluid can be obtained from equation (4.1) presented in § 1.2:

$$W_t \cdot \Delta t = -(u_1 - u_2)\dot{m} \cdot \Delta t + E(t + \Delta t) - E(t) \tag{4.1}$$

In steady state conditions the energy owned by the fluid inside the thermal probe ($E(t)$) is practically constant. In these conditions the term $E(t + \Delta t) - E(t)$ is negligible. Thus the equation can be written in the form:

$$W_t \cdot \Delta t = -(u_1 - u_2)\dot{m} \cdot \Delta t$$

and simplifying the time interval:

$$W_t = -(u_1 - u_2)\dot{m}$$

The internal energy of water, in the range of variability of pressure inside the thermal probe ($150 \pm 5kPa$), varies mainly with temperature, according to the following law:

$$u(T, p = 150kPa) = 4.181832 \cdot T + 0.386592$$

The unit of measurement of u is $\frac{kJ}{kg}$.

Thus, the equation can be written:

$$W_t = -[(4.181832 \cdot T_{_1} + 0.386592) - (4.181832 \cdot T_{_2} - 0.386592)]\dot{m}$$

Then:

$$W_t = -4.181832 \cdot (T_{_1} - T_{_2})\dot{m}$$

And finally:

$$T_{_1} - T_{_2} = -(\frac{W_t}{4.181832 \cdot \dot{m}}) \cdot (\frac{1}{1000})$$

Substituting the values of the estimated thermal power of the probe and of the mass flow rate, the following is obtained:

$$T_{_1} - T_{_2} = -\frac{-19.50}{4.181832 \cdot 0.42} \cdot \frac{1}{1000} = 0.0111 \backsimeq 0.01K$$

This estimated temperature difference is lower than the sensitivity of the temperature sensors that is of the order of $0.05K$.

4.3.2 Temperature Field Inside The Control Volume

The temperature field in the control volume, as a function of time, is described using the axial symmetry hypothesis (§ 4.2). The boundary conditions are defined for the external surface of the thermal probe and for the six lateral surfaces of the experimental apparatus.

At the external surface of the thermal probe has been given the temperature of the fluid inside the thermal probe, assuming a linear temperature distribution of the fluid from the entry section to the exit section.

The temperature used for the boundary conditions on the lateral faces of the control volume is the average initial temperature inside the control volume. This choice provides that the material inside the control volume is in equilibrium with the external environment and that the environment temperature is sufficiently stable in time (Figure 4.1).

The boundary conditions at the upper and lower face are approximated with the temperature measured by the sensors located in the proximity (at 50 mm and at 900 mm from the bottom, Figure 2.7).

The Inverse Distance Weighted Interpolation Method

The Inverse Distance Weighted (IDW) method is a deterministic method for multivariate interpolation of a scattered set of known points. A deterministic method treats the bonding between nearby points using an explicit law whose parameters have physical meaning. The assigned values to unknown points are calculated using a weighted average of the values assumed by the

known points. The weight of the values at the known points depends on their distance from the unknown point whose value has to be calculated and the *power parameter "p"* as follows: $\omega_i(X) = \frac{1}{d(X, X_i)^p}$, where $\omega_i(X)$ is the weight of the value of the point X with respect to the point X_i whose value has to be determined. $d(X, X_i)$ is the distance between the two points and p is the power parameter (Shepard, 1968).

The influence of p is presented in Figure 4.35 where *power parameters* of 0, 1 and 2 are considered. As shown, if p equals to 0 all the weights of each known value $\omega_i(X)$ are worth 1, if p is 1 then $\omega_i(X)$ decreases with distance from the unknown point so that more distant points have less weight, if a higher p of 2 is used further away points have even less weight.

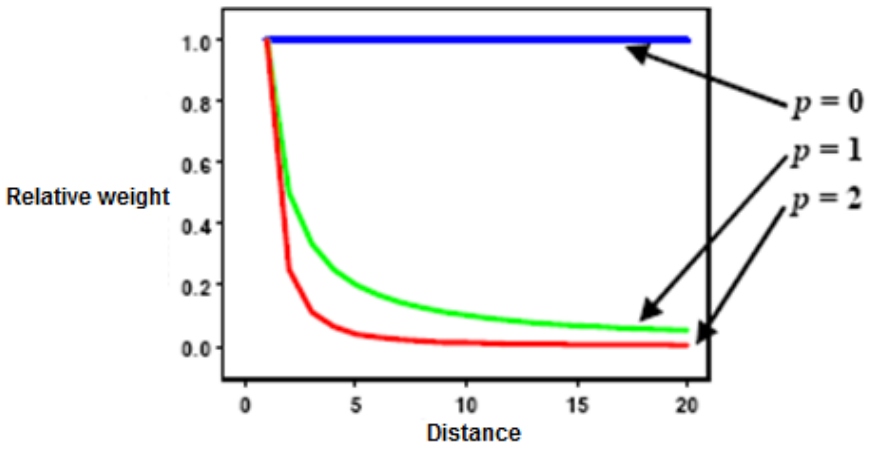

Figure 4.35: Influence of the power parameter p on the weight of values attributed to known points at different distances from the unknown point whose value has to be calculated (R. Singh, J. Ferreira, Massachusetts Institute of Technology Department of Urban Studies and Planning, 2019).

Temperature Field Plots

The Figures 4.36 and 4.37 show the temperature field inside the control volume after various time instants from the beginning to the end of the test. The colors represent different temperatures as suggested by the legend on the right of the figures. The temperature is considered relative to the average initial temperature inside the control volume.

One can note that the temperature field grows very rapidly at the beginning of the test and gradually slower with time, in fact it is detectable that already halfway through the time of the test the temperature field (t = 200000s) is very near to the one referred to the end of the test (steady state conditions) at t = 438816s (Figure 4.37).

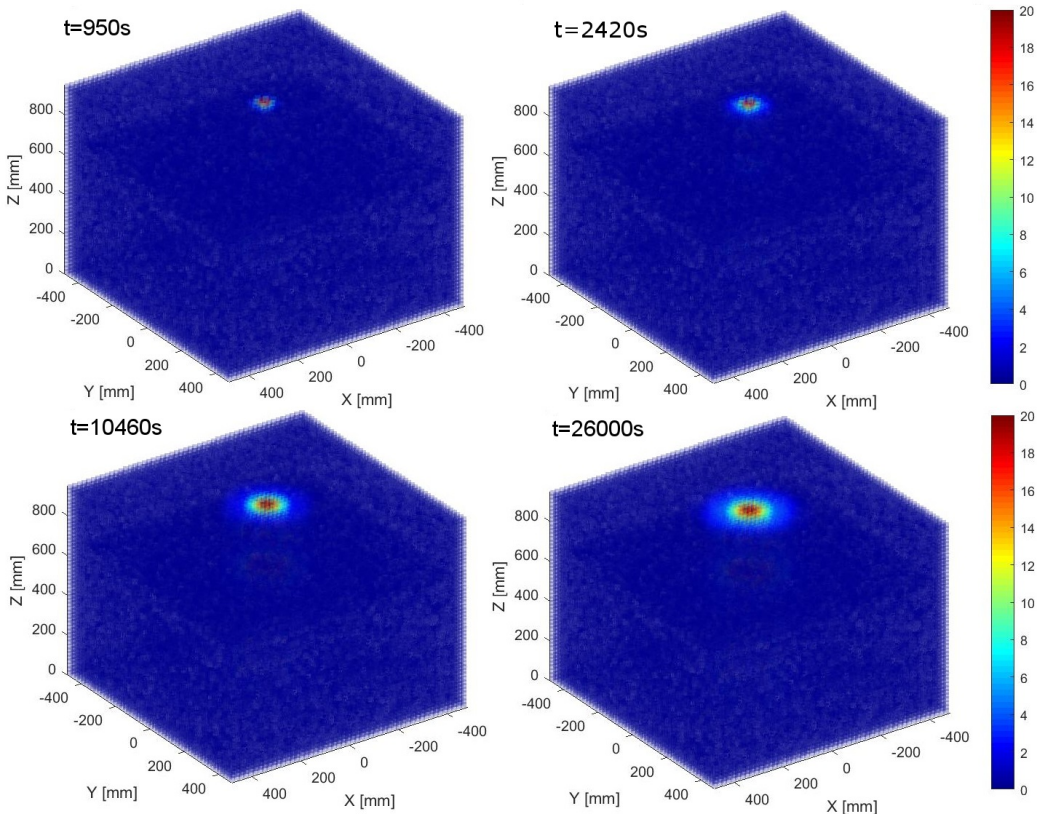

Figure 4.36: Temperature field inside the control volume after 950, 2420, 10460 and 26000 seconds from the beginning of the test.

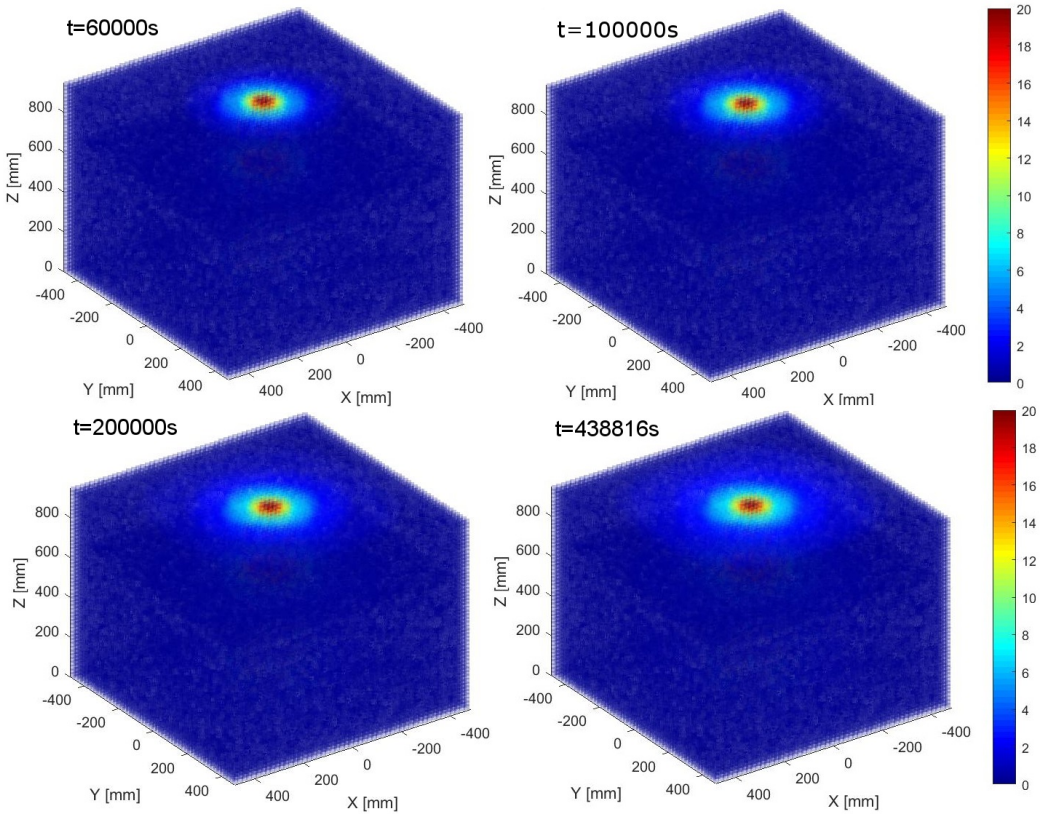

Figure 4.37: Temperature field inside the control volume after 60000, 100000, 200000, 438816 seconds from the beginning of the test.

In Figure 4.38 are displayed two vertical slices, obtained with the Matlab scatteredinterpolant function, containing the thermal probe axis along x and y axes. The colors represent different temperatures as suggested by the legend to the right of the figure. The temperature is considered relative to the average initial temperature inside the control volume.

A lobed profile is evident at any time considered, nevertheless the axial symmetry with respect to the probe axis is appreciable. This lobed profile persists regardless of the power parameter p adopted in the IDW method (in this case $p = 2$) and indicates that a better distribution of points with known temperature has to be chosen, using the symmetry hypothesis.

Another aspect that can be caught is that the great majority of thermal energy is located in the immediate vicinity of the thermal probe, that is coherent with the heat conduction theory in case of a cylindrical geometry (equation (1.7)). The area interested by the thermal wave, in fact, is bigger as the distance from the probe grows leading to a logarithmic behavior.

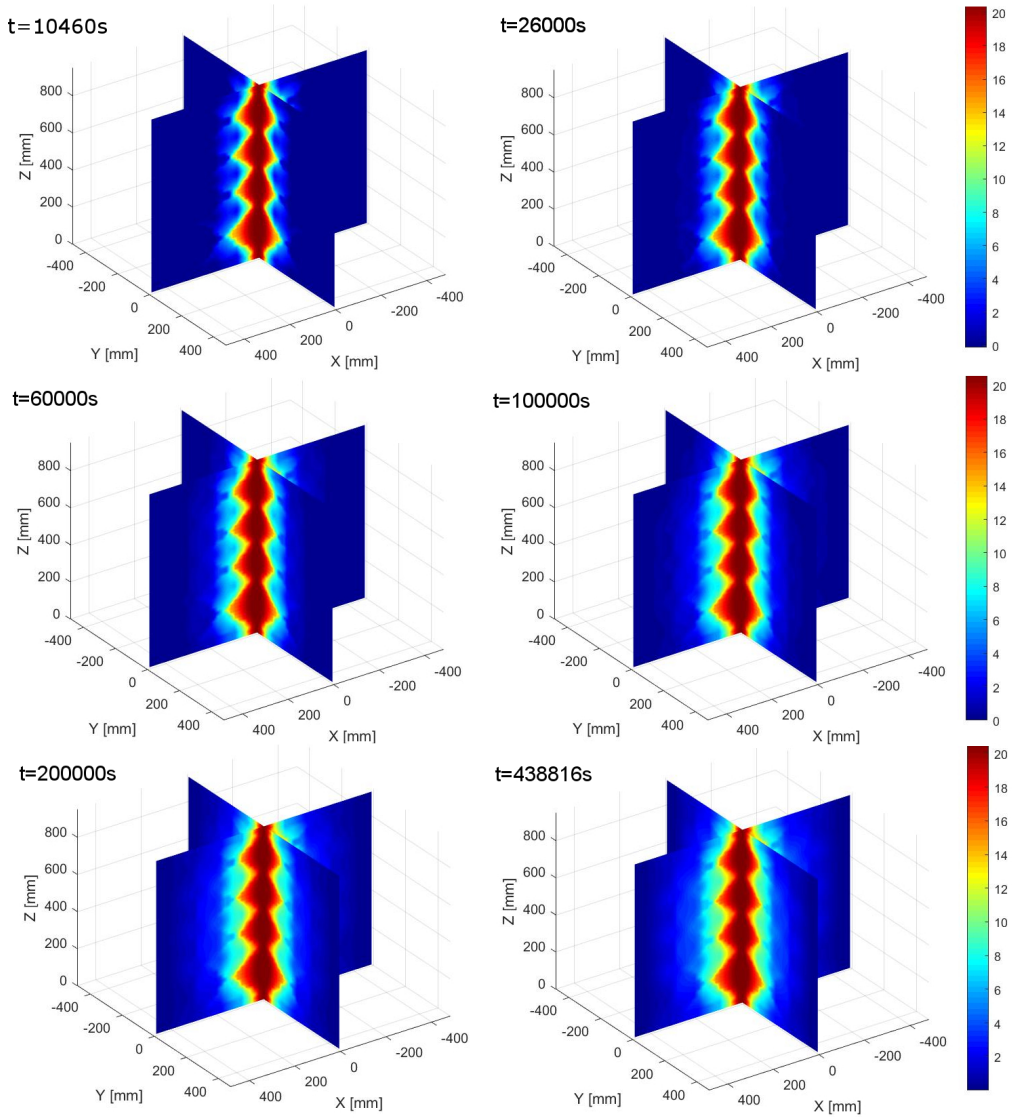

Figure 4.38: Temperature field on vertical slices along x and y axes of the control volume after 10460, 26000, 60000, 100000, 200000 and 438816 seconds. Both slices contain the z axis.

Chapter 5

Conclusions

- The first aspect to consider is the legitimacy of the axisymmetric behavior hypothesis with respect to the thermal probe axis, since that hypothesis is used for the temperature field determination. In the test configuration this hypothesis is valid, as Figures 4.2 and 4.3 display;
- The steady state conditions can be interpreted with Fourier's equation derived in cylindrical coordinates (equation (1.8));
- In Subsection 4.3.1, it has been concluded that the main process of thermal energy transfer inside the control volume, at the test conditions, is thermal conduction. In fact, the behavior of the granular material-intergranular fluid, assumed as an homogeneous and isotropic material, can be described using the conduction equations. There may be some convection and radiation effect, if so they are small and not significant;

- The exchanged thermal energy tends to make the internal energy of the granular material grow, especially near the thermal probe, with a logarithmic reduction law as the distance from the thermal probe increases;

- The steady state conditions are reached after a very long time, of the order of 5 days;

- The temperature difference detected at the extremes of the thermal probe (see Figure 2.3) has values that are of the same order of magnitude as the sensitivity of the temperature sensors (of the order of $0.05K$). It is not reasonable, under these experimental conditions, to apply the procedures illustrated in § 1.2 to evaluate the power of the probe. This can be evaluated both on the basis of the knowledge of the thermodynamic properties of the material, obtained by other experimental tests performed with the use of water as intergranular fluid, and by calibrating numerical models that reproduce the experimental test;

5.1 Future Developments

The model has also been designed to conduct tests with water as a intergranular fluid and with filtration motion. Some of these tests have already been performed and are in the process of interpretation.

More tests must be performed with different materials from the *Risetta*

del Brenta, also in order to evaluate the effects of natural convection, which appear to be significantly present in the first tests with water.

The physical model can be declined in a lot of different designs in terms of material and fluid within the control volume, type and material of the thermal probe and distribution of temperature sensors. An example could be the simulation of the presence of a stratified terrain, buried bodies or discontinuities, and their effect on the physical processes that take place when a thermal probe exchanges energy with the surrounding environment.

Currently, geostatistical interpolation techniques are being applied for the calculation of the temperature field within the control volume. More precisely, the Kriging interpolation method seems to work fine, but the results still need to be validated.

The experimental apparatus appears to be improvable in the temperature detection and acquisition system. The validation of the detected temperature data requires, at the moment, a long time.
Another possible improvement is a better insulation of the top and bottom part of the control volume in order to limit the loss of energy.

The physical model can be useful in order to better understand the role of the different physical parameters involved in the phenomena of heat exchange. It can be a powerful tool for the characterization of materials and different designs of a heat exchanger. The experimental data from the physical model in object can be also useful in the compilation and calibration of numerical models.

Aknowledgments

The author wishes to thank Paolo Scotton for the patience and the diligence during the review of this work and Simonetta Cola, head of the Geotechnical Engineering Laboratory, DICEA, University of Padua, where the experimental set up is installed.

References

Al-Khoury, R., & Bonnier, P. (2006). Efficient finite element formulation for geothermal heating systems. part ii: transient. *International Journal for Numerical Methods in Engineering*, *67*(5), 725–745.

Al-Khoury, R., Bonnier, P., & Brinkgreve, R. (2005). Efficient finite element formulation for geothermal heating systems. part i: Steady state. *International journal for numerical methods in engineering*, *63*(7), 988–1013.

Carlini, M., Castellucci, S., Allegrini, E., & Tucci, A. (2012). Down-hole heat exchangers: modelling of a low-enthalpy geothermal system for district heating. *Mathematical problems in engineering*, *2012*.

Fourier, J. (1955). *Analytical theory of heat, english translation by a.* Freeman, Dover Publications, New York.

Green, D. L. (2014). 5.3. modelling geomorphic systems: Scaled physical models.

Philippe, M., Bernier, M., & Marchio, D. (2009). Validity ranges of three analytical solutions to heat transfer in the vicinity of single boreholes. *Geothermics*, *38*(4), 407–413.

Scotton, P. (2017). Un apparato sperimentale per lo studio dello scambio energetico tra sottosuolo e la sonda geotermica.

Scotton, P., Teza, G., Rossi, D., Dalla Santa, G., & Galgaro, A. (2018). Experimental setup to measure the heat-exchange processes by controlling thermal and hydraulic conditions.

Shepard, D. (1968). A two-dimensional interpolation function for irregularly-spaced data. In *Proceedings of the 1968 23rd acm national conference* (pp. 517–524). New York, NY, USA: ACM. Retrieved from `http://doi.acm.org/10.1145/800186.810616` doi: 10.1145/800186.810616

Sutton, M. G., Nutter, D. W., & Couvillion, R. J. (2003). A ground resistance for vertical bore heat exchangers with groundwater flow. *Journal of Energy Resources Technology*, *125*(3), 183–189.

Talleri, M. (2001). Applicazioni geotermiche negli impianti di attivazione termica della massa. *Seminari Velta*, *2001*(2).

Volkov, A., Ryzhenkov, A., Kurshakov, A., Grigoriev, S., & Bekker, V. (2017). Physical modelling of temperature's potential decrease for near-wellbore rocks during extraction of thermal energy. *International Journal of Applied Engineering Research*, *12*(17), 6570–6575.

Wang, Y., Gao, Q., Zhu, X., Yu, M., & Zhao, X. (2013). Experimental study on interaction between soil and ground heat exchange pipe at low temperature. *Applied Thermal Engineering*, *60*(1-2), 137–144.